crystals

MDPI

Article

Quasi-Liquid Layer on Ice and Its Effect on the Confined Freezing of Porous Materials

Qiang Zeng [1] and Kefei Li [2,*]

[1] College of Civil Engineering and Architecture, Zhejiang University, Hangzhou 310058, China; cengq14@zju.edu.cn
[2] Department of Civil Engineering, Tsinghua University, Beijing 100084, China
* Correspondence: likefei@tsinghua.edu.cn; Tel.: +86-10-62781408

Received: 31 March 2019; Accepted: 6 May 2019; Published: 14 May 2019

Abstract: Freezing of the water confined in thin pores can be destructive to the porous frame, but the effect of the quasi-liquid layer (QLL) between the confined ice and the pore walls remains still far from being fully understood. In the present study, the physical origins of the intermediate phase of QLL were discussed by thermodynamic analyses. Different interactions on QLL bring different models to estimate its thickness, which generally decays with temperature decreasing. Four representative models of QLL thickness were selected to unveil its effect on the growing rates and extents of ice in a concrete. The engineering consequences of the confined freezing were then discussed in the aspects of effective pore pressures built from the confined ice growth and deformations framed by a poro-elastic model. Overall, thickening QLL depresses ice growing rates and contents and, consequentially, decreases pore pressures and material deformations during freezing. The QLL corrections also narrow the gaps between the predicted and measured freezing deformations. The findings of this study contribute to profound understandings of confined freezing that may bridge over physical principles and engineering observations.

Keywords: freezing; quasi-liquid layer; pressure; deformation

1. Introduction

Since the first postulation of a quasi-liquid layer (QLL) on ice over 160 years ago, the understandings of its structure and links to our daily life (e.g., skating on ice and anti-freezing agent to keep food fresh) have been increasingly advanced [1–5]. Generally, this QLL, depending on the environmental temperature and what media ice is exposed to, ranges from one to several water molecular layers [6–13]. Predicting the thickness of QLL always faces challenges especially when the phase transition from water to ice is beyond the bulk freezing. A pertinent example is the freezing of the water confined in thin pores, which can be influenced by many factors such as the geometry confinement that regulates the crystal anisotropy, the curvature effect that depresses the freezing temperature, and the actions of the pore walls on the pore fluid [1,3,11,14–17]. Indeed, in chemical, environmental, and civil engineering, the confined freezing is more frequently quoted because almost all materials (except pure metals and crystals) are, more or less, in porous structures, and the phase transition of the water confined in the pores may occur in certain conditions during freezing [3,18]. However, the understandings of the possible influences of QLL on the freezing process of the confined water and the engineering consequences remain far from being completed.

To date, great efforts have been made to accumulate the knowledge of confined freezing by advanced experiments and simulations [6–12,19,20]. An example of the corresponding achievements may be the continually-developed cryoporometry techniques that allow us to measure the pores at nano-scales with the corrections of QLL [19,21]. As a typical porous material, concrete (and other

cement-based materials like cement paste and mortar) may perform at low temperature, and confined freezing will occur in the material. However, the research on the role QLL plays and its effects on the mechanical consequences of concrete has been limitedly reported [20,22–24]. In the present study, attempts were made to address how and to what extent the QLL between ice and the pore wall affects the confined freezing of a porous concrete.

In what follows, physical bases for confined freezing are briefly reviewed to display the generalized links between QLL thickness and temperature. The QLL data were collected from comprehensive experiments and simulations. Four different models of QLL thickness were then selected to demonstrate the QLL effect on the ice rising rates and contents in a porous concrete sample. Those QLL data were then implanted into a poro-elastic model to unravel the influences of QLL on the pore pressures built by ice crystallization and, consequentially, the material deformations. The scope of this study strictly followed the classic physico-chemical regimes of water, ice, pore confinement, and their interactions, and some simplifications of the properties of those phases were necessitated. The results of this study shed light on the understandings of the engineering consequences of confined freezing occurring in porous materials.

2. Physical Bases for Confined Freezing

2.1. Freezing in Pores

Physically, to form ice crystals in either bulk or confined water, the free energy (or chemical potential) of the ice must be lower than (or at least equal to) that of the liquid water. Here, we assumed that ice crystals can spontaneously form in the pores once the ice-water equilibrium was reached, and the kinetic issues (e.g., ice nucleation and water supercooling [25]) are out of the scope of this study. Figure 1 illustrates a snapshot of a partially-freezing pore network at a subzero temperature. For simplification, only a coarse pore chamber with two thin pore entries (or throats) is demonstrated in the figure. As displayed in Figure 1, ice occupies the pore chamber with a unique QLL in the thickness of t between the ice and the pore wall. Due to the curvature effect of the pore, which can lower the free energy of the confined water, freezing takes place at a depressed temperature, which can be described by the Gibbs–Thompson (GT) equation [19],

$$T_0 - T_m = \frac{2\kappa T_0 \gamma_{cl}}{\Delta H_f} \tag{1}$$

where T_m (K) is the melting temperature in equilibrium; T_0 (K) is the bulk freezing temperature of water in the standard condition ($P = 1$ atm); κ (1/m) is the mean curvature of the pore; γ_{cl} (N/m) is the surface tension of ice exposed to liquid water; ΔH_f (J/m^3) is the fusion enthalpy. The GT equation has been extensively applied to capture the shifts in freezing temperature of pore fluids confined in various porous materials [19,20,22].

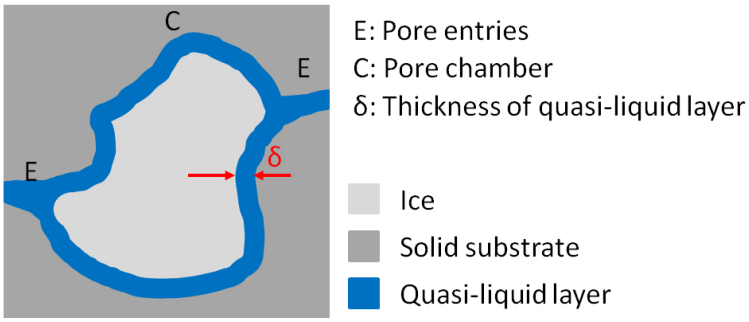

Figure 1. Cross-sectional view of a pore filled with an ice and connected with small entries. A quasi-liquid layer (QLL) with a thickness of t between the ice and the pore wall exists to achieve a physico-chemically-stable status of the confined freezing system.

Due to the complex pore networks of porous materials [26], even if the thickness of QLL is known, it remains difficult to estimate the ice volume due to the complex pore geometry and anisotropy. Here, we assumed that the partially-frozen pores are convex in principle, then the volume V and surface area A of the pores and the confined ice crystals that are separated by the QLLs can be estimated by [27],

$$V_c = V_p - A_p\left(t - \kappa t^2\right) \tag{2a}$$

$$A_c = A_p\left(1 - 2\kappa t\right) \tag{2b}$$

where the subscripts p and c denote the pores and ice crystals, respectively. Here, the mean pore curvature κ can be determined by the principle radii of curvature r_1 and r_2 through $\kappa = (A/2)\int(1/r_1 + 1/r_2)\mathrm{d}r$ [28]. Once the pore geometries in a porous material were identified, Equation (2) helped build an integrated equation to estimate the ice content in the porous medium during freezing.

2.2. QLL on Ice

A disordered phase will exist on a solid ice surface in equilibrium if it can lower the free energy of the system; that is, if by its existence, an intermediate layer of thickness, t, reduces the total excess free energy. Physically, in an ice-QLL-substrate system, the total free energy changes come from (1) the heat release by ice formation, (2) the formation of a new liquid-crystal surface, and (3) the energy disturbance by the sandwich-like ice-QLL-substrate structure [3,4,27].

The thickness of QLL between ice and substrate, t, is intrinsically related to its potential, $F(t)$, which depends on the acting forces between the solid-liquid and liquid-ice interfaces [4,14]. The thermodynamic bases for the relationships between F and t can be found in Appendix A. There are several regimes governing the acting forces on the intermediate QLL phase. One widely-adopted regime is that the forces decay exponentially with the distance between the ice and substrate surfaces [3,14,19], i.e., $F = 1 - \exp(-2t/\varepsilon)$, with ε being the characteristic decay length, which can be determined by experiments [6]. In this case, the QLL thickness can be expressed as,

$$t = \frac{-\varepsilon}{2}\ln\left[\frac{\varepsilon\Delta H_f\left(T_m - T\right)}{2T_0\Delta\gamma}\right] \tag{3}$$

where $\Delta\gamma$ (N/m) is the surface energy differences when the supposed substrate-crystal (sc) interface is replaced by the liquid-crystal (lc) and liquid-substrate (ls) ones (that is, a QLL inserts between the ice and the pore wall shown in Figure 1) and can be expressed as $\Delta\gamma = \gamma_{sc} - (\gamma_{lc} + \gamma_{ls})$. Equation (3), indeed, conforms to the well-used approximating form, $t \propto \ln(T_m - T)$, for representing the $t - T$ relation [14,19,29].

However, there may exist complex physical actions on the QLL phase, e.g., the long- and short-range electrostatic, nonretarded, and retarded van der Waals interactions [3]. Depending on the sorts of interactions, Wettlaufer et al. [30] suggested a generalized power decaying equation of the interfacial potential $F(t)$, $F = t^n/\left(t^n + \sigma^n\right)$, with σ being a typical interatomic distance. In general, σ is far lower than t ($\sigma \ll t$), and the potential decaying equation can be simplified to $F \approx 1 - (\sigma/t)^n$. In the case of the power decaying function of the potential, the QLL thickness can be given by:

$$t = \left[\frac{\Delta H_f\left(T_m - T\right)}{n\Delta\gamma\sigma^n T_0}\right]^{-1/(1+n)} \tag{4}$$

If, for instance, the interfacial actions between two microscopic bodies in a limiting separation are dominated by the long-range electrostatic forces, whose long-range potential decays with the square of the distance ($n = 2$), $F = t^2/\left(t^2 + \sigma^2\right) \approx 1 - \sigma^2/t^2$, Equation (4) then reduces to,

$$t = \left[\frac{\Delta H_f\left(T_m - T\right)}{2\Delta\gamma\sigma^2 T_0}\right]^{-1/3} \tag{5}$$

In fact, Equation (5) captures the well-used semi-empirical model for estimating the thickness of QLL on ice, $t \propto (T_m - T)^{-1/3}$ [31].

2.3. Discussion on QLL Data and Models

The continually-developed experimental and simulative techniques have greatly accumulated our knowledge of the molecular structures of QLL and its thickness. Figure 2 illustrates the QLL thickness data acquired from the literature [6–12,19,29,31–36]. When dealing with those data, we ranked the data by author and neglected the thickness differences in different crystal faces, despite that surface melting takes place anisotropically on ice crystal surfaces [1,11].

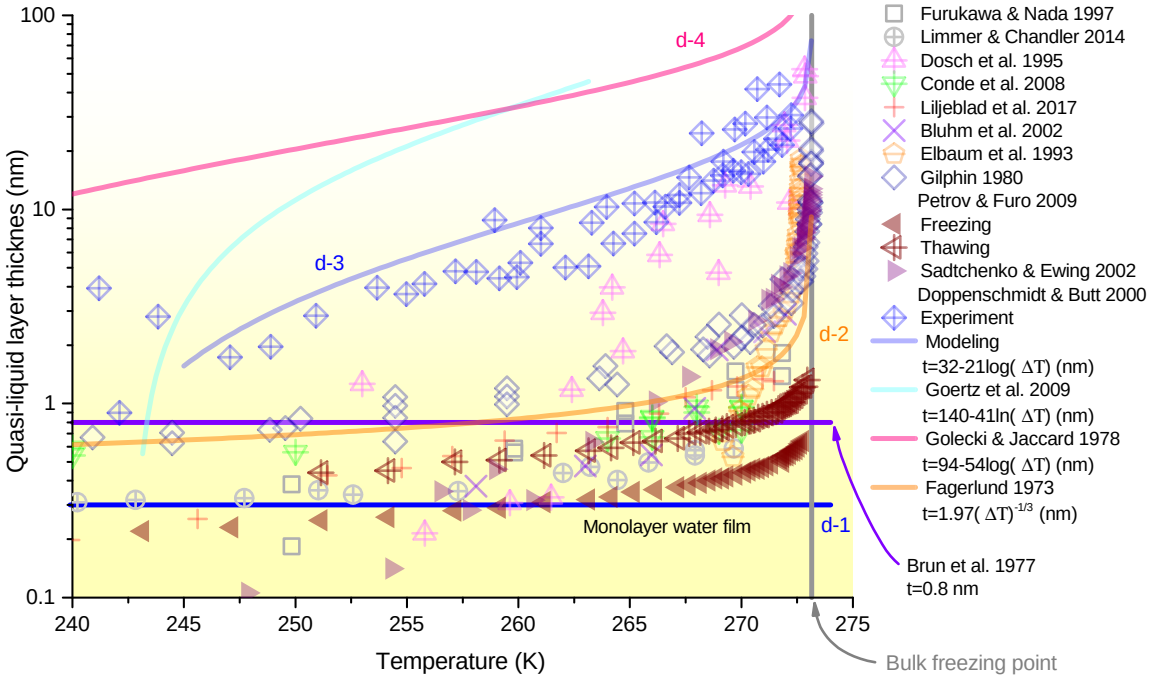

Figure 2. QLL thickness data from the literature [6–12,19,29,31–36]. The QLL thickness data reported in Furukawa and Nada (1997) [11], Conde et al. (2008) [10], and Limmer and Chandler (2014) [7] were obtained by molecular dynamic simulations; those in Elbaum et al. (1993) by interference microscopy; those in Dosch et al. (1995) [12] by glancing-angle X-ray scattering; those in Gilpin (1980) [36] by theoretical calculation; those in Doppenschmidt and Butt (2000) [6] by atomic force microscopy; those in Bluhm et al. (2002) [8] by photoelectron spectroscopy; those in Sadtchenko and Ewing (2002) [34] by infrared spectroscopy; those in Petrov and Furo (2009) [19] by thermodynamic estimations; and those in Liljeblad et al. (2017) [9] by total internal reflection Raman, vibrational sum frequency, and NMR spectroscopies. The $t - T$ line reported in Goertz et al. (2009) [33] was regressed from the experimental data measured by interfacial force microscopy and that in Brun et al. (1973) [32] by differential scanning calorimetry. The $t - T$ curves of d-1, d-2, d-3, and d-4 are representatively selected for unraveling the influences of QLL on freezing of porous materials; see Table 1.

At first glance, from Figure 2, the QLL thickness varied by up to three orders of magnitude for a set temperature, depending on the measurements. A primary factor that dominates the QLL thickness may be the different methods used to detect the QLL phase on ice and to measure its thickness. For instance, Golecki and Jaccard [29] employed a channeling technique of nuclear backscattering that is sensitive to crystalline imperfection to detect the thickness of QLL on pure ice and found rather large values of the QLL thickness (e.g., ≈100 nm at −1 °C); while Doppenschmidt and Butt [6] measured the QLL thickness on ice surfaces by atomic force microscopy (AFM) and obtained much thinner data (e.g., ≈32 nm at −1 °C). Another dominative factor may be the surfaces with which ice crystals are in contact. Indeed, experimental studies have demonstrated that the thickness of the QLL between ice

and amorphous SiO_2 is always less than 10 nm [9,37]. Last but not least, the impurities of ice will also impact the surface melting and its thickness [18]. An AFM measurement on ice containing 10 mM KCl indicated that the QLL on the contaminated ice is much higher than that on pure ice [6]. For more data and discussions about QLL, the readers may refer to the comprehensive reviews [3,14,18] and a book chapter [1].

Since the thickness of QLL on ice is dominated by the actions on the intermediate phase, different physical interactions can induce different models (see for instance the models shown in Section 2.2). Indeed, those physical interactions depend on the surfaces to which ice crystals are exposed. For example, a theoretical study by Wettlaufer et al. [30] revealed that the premelting behavior of the ice confined in soils is beyond the classic van der Waals interactions, rather in the regime of the long-rang electrostatic interactions. This means that the potential-distance function can be represented by $F = 1 - \sigma^2/t^2$, so the thickness of the QLL on the soil-confined ice roughly conforms to Equation (5). Moreover, it was implied that the exponential decaying regime may be suitable to estimate the QLL thickness for freely-exposed ice crystals (Equation (3)), whereas the power decaying regime for those in contact with solid surfaces (Equation (4)) [14]. However, experimental data (e.g., [37]) suggested that the QLL between ice and SiO_2 substrate also conforms to the logarithmic law, $t \propto \ln(T_m - T)$. The data recalled in Figure 2 also imply that both the exponential and power decaying regimes may capture the same $t - T$ data to some extent.

One may also integrally consider both the short-and long-range potentials of the QLL on ice [4], which, however, will bring two inevitable troubles in assessing its thickness. The primary one is that the explicit and simple expressions like Equations (3) and (5) cannot be obtained, and complex numerical calculations are required. The other one is that the parameters of both the short-and long-range potentials are rather difficult to obtain, because how they work in establishing the QLL phase on a surface remains an open question [13]. Here, therefore, the simply uncoupled short-and long-range potentials are discussed to unravel the physical regimes of the QLL on ice.

Table 1. Selected $t - T$ curves.

Item	Value (nm)	Method	Ref.
d-1 (lower bound)	$t = 0.3$	Monolayer water molecule	[3]
d-2	$t = 1.97\|\Delta T\|^{(-1/3)}$	Estimated from sorption data	[31]
d-3	$t = 32 - 21\lg(\Delta T)$	Measured by AFM	[6]
d-4 (upper bound)	$t = 95 - 54\lg(\Delta T)$	Estimated by proton channeling	[29]

To elucidate the influences of QLL on the freezing behaviors of porous materials, we here representatively selected four $t - T$ curves, i.e., d-1 (monolayer water molecule), d-2 (power decay of the QLL potential, long-rang interaction), d-3, and d-4 (exponential decay of the QLL potential, short-range interaction) marked in Figure 2 and listed in Table 1. Specifically, the size of the monolayer water molecule (d-1) was set as the lower bound of the QLL thickness, even though it is not necessary to limit the QLL thickness [9]. The d-4 curve was set as the upper bound of the QLL thickness. We shall understand that the selected $t - T$ curves may not strictly conform to the freezing regimes we will discuss (i.e., freezing in pores); however, the interpretations on confined freezing with the QLL in different thickness models will shed much light on the engineering consequences of freezing where this intermediate phase is often ignored.

3. Ice Content in Porous Media

3.1. QLL-Modified GT Equation

One of the core issues concerning freezing in porous media is the ice content in the pores at a subzero temperature, which is vitally important due to the significant engineering consequences (e.g., weathering of stones and damage of buildings and infrastructures). Following the GT equation

and assuming that the freezing of water occurs in a cylindrical pore with radius r_p, we can rewrite Equation (1) as,

$$r_p = r_c + t = \frac{2T_0\gamma_{cl}}{\Delta H_f\left(T_0 - T_m\right)} + t \tag{6}$$

Here, the possible water-QLL-ice contact-line effect was not considered (if it exists). This expression suggests that the presence of QLL in thickness t can further depress the equilibrium temperature for ice formation in a confined space, as the curvature of the confined ice is altered by the QLL ($\kappa = 1/\left(r_p - t\right)$).

Figure 3a shows in what pore sizes the confined water can freeze under a certain temperature depression when different datasets of QLL thickness (Table 1) are employed. When plotting Figure 3, a constant value of $2T_0\gamma_{cl}/\Delta H_f \approx 30$ nm · K was employed [19]. At a subzero temperature, thickening the QLL tends to enlarge the pore radius to accommodate the ice that should always match the pore curvature in equilibrium. This effect is more significant for the freezing in nanopores [15,38]. If we considered a pore with a radius of 100 nm, which is rigid (no frame deformation) and pre-saturated with water, then the ice content ($= (r-t)^2/r^2$ for cylindrical pores) would vary with the QLL thickness. As displayed in Figure 3b, ice occupies the whole pore in the cases of non-QLL and the QLL thickness of d-1 once the temperature drops to around -0.302 °C. For the QLL thickness of d-2, which remains insignificant, the ice content instantaneously rises to around 96% at -0.305 °C and then increases slightly due to the continual decrease in the QLL thickness. When the d-3 model of QLL thickness is used, the freezing temperature is depressed to around -0.53 °C because the QLL-corrected size for ice is sharply narrowed to around 62 nm at this temperature; and the instantaneous ice content is depressed as well ($\phi_c = 0.62^2 = 0.38$). When the $t - T$ curve is governed by the d-4 model, the freezing temperature and the instantaneous ice content become -1.72 °C and 0.03, respectively (Figure 3b). Due to the continually-thinning process of the QLL with the depressed temperature, the ice content continually increases.

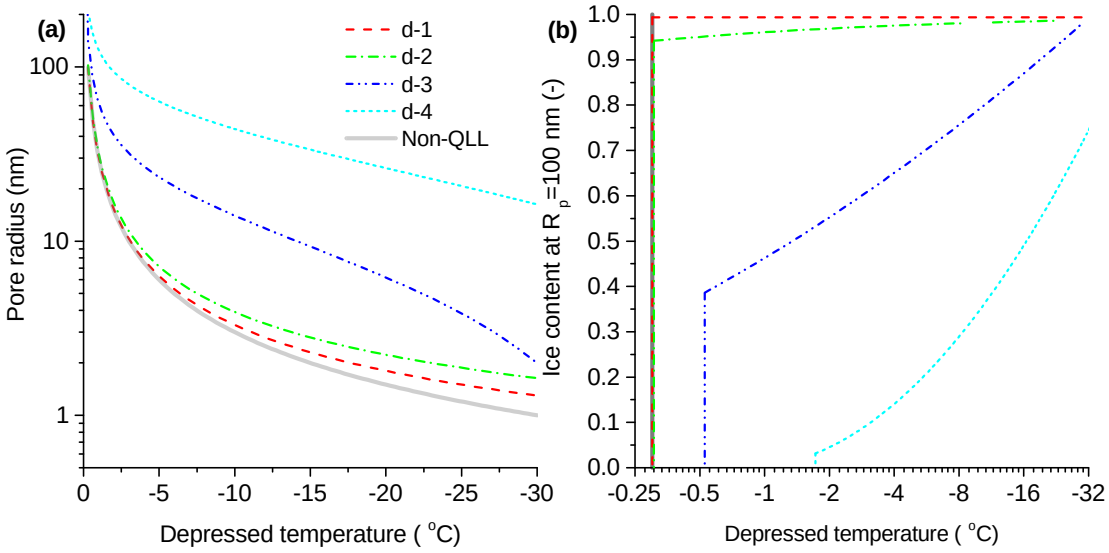

Figure 3. (**a**) The plots of pore radius against depressed temperature predicted by the Gibbs–Thompson (GT) equation with different datasets of QLL thickness; (**b**) the variation of ice content with depressed temperature in the pore of 100 nm.

Note that the real pore structure of porous materials would be much more complex than the simply mono-sized and cylindrical pores; therefore, the ice content would be also beyond the results displayed in Figure 3b. For macroporous and mesoporous materials, the contribution of the QLL to the ice (or liquid) fraction would be small relative to that of the GT effect [3,39]. For nano-porous materials, like porous silica [38], the QLL contribution cannot be neglected. Furthermore, for porous building

materials, e.g., cement-based materials that show very broad pore ranges from nano- to macro-sizes, the QLL effect may play its part at different pore scales to different extents. Furthermore, the value of $2T_0\gamma_{cl}/\Delta H_f$ may change with different surface and curvature conditions (21–53 nm·K [19]), but the specific value will not change the main observations displayed in Figure 3.

3.2. Pore Structure Associated Ice Content

We here took a real concrete sample as an example to demonstrate the QLL effect on the ice content in porous materials under freezing. The pore structure of the concrete was determined by mercury intrusion porosimetry (MIP). The MIP porosity and total porosity (in reference to the status of the sample dried at 105 °C) were 0.138 and 0.181, respectively. With the maximum mercury intrusion pressure of 414 MPa, the contact angle between the pore wall and mercury front of 130 ° and the surface tension between vapor and liquid mercury of 485 N/m, the pore size distribution (PSD) of the concrete sample can be obtained by the Washburn equation [40]; see the insert panel of Figure 4. Clearly, multiple peaks in the PSD curve can be observed due to the fact that different pores at different scales integrally dominate the pore spatial distribution. The pore peak around 10 μm (marked A in the insert panel in Figure 4) may denote the coarse capillary pores between the cement clinkers and the coarse pores in the interfacial transition zone (ITZ) between the aggregates and the cement matrix. The pore peak at 200 nm (marked B) may represent the capillary pores between the cement hydrates (or termed as the inter-particle space [41]). The peak at the thinner size (marked C) may reflect the thin capillary pores and coarse gel pores: the space between the layered C-S-H gel clusters. One shall understand that the very fine interlayer pores (<1 nm) cannot be detected by MIP [42]. Last but not the least, the pore structure measured by MIP may be biased by the oversimplified assumptions of the pore geometries and the physical principles (the Washburn equation) applied for the test.

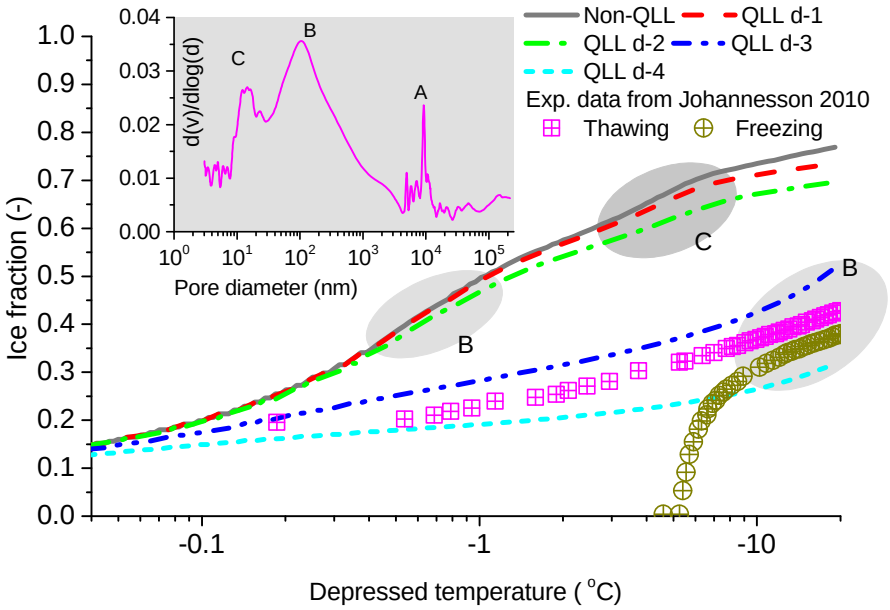

Figure 4. Ice fractions of a concrete sample (water to cement ratio of 0.6) under freezing estimated by the GT equation with the selected QLL models and the experimental ice content reported in [43]. The insert panel is the pore size distribution of the concrete determined by mercury intrusion porosimetry (MIP) with the marks A, B, and C, respectively, representing the coarse pores, capillary pores, and gels pores in the concrete sample. The shadowed areas with the same marks denotes the consequences of ice formation in those pores.

The ice content of the concrete sample can be estimated by the GT equation (Equation (6)) with the PSD data. Again, assuming that the penetration of ice in any pore is strictly under thermodynamic equilibrium and neglecting the possible effect of the ions in the pore fluid [44], the accumulative ice content ϕ_c at a temperature T can be given by:

$$\phi_c = \int_{T_0}^{T} \frac{\partial \phi_c}{\partial T} dT = \int_{T_0}^{T} \frac{\partial \left[\int_{\infty}^{r_p^{GT}} \frac{\partial \phi_p}{\partial r_p} \left(1 - \frac{t(T)}{r_p}\right)^2 dr \right]\Big|_{r_p - t \geq r_c}}{\partial r_c} \frac{\partial r_c}{\partial T} dT \quad (7)$$

where r_p^{GT} denotes the minimum pores in which ice can penetrate under the GT equation. In Equation (7), all parameters are known except for $\partial \phi_p / \partial r_p$, which can be read from the MIP PSD data. The expression in the square brackets represents the changes in ice content induced by both the filling of new pores and the thinning of QLLs. The readers may find some alternative methods to Equation (7) for estimating the ice content of porous materials under freezing by different porosimetries (e.g., [24,45,46]). In this study, because the minimum accessible pore radius of the MIP test was 1.5 nm, which yielded the required lowest temperature by the GT equation of −20 °C, the analyses thus stopped at this temperature.

Figure 4 shows the ice contents of the concrete sample with the selected QLL models. At first glance, the existence of QLL will always decrease the ice fraction at any subzero temperature, and the thicker is the QLL, the lower is the ice fraction. These can be reasonably understood as the supposed ice phase that is adjacent to the pore walls is replaced by the interfacial QLL phase. Due to the significant sensitivity of the ice front size to the depressed temperature in equilibrium, a very slight deviation of the temperature from the freezing point will cause a heavy filling of ice in the pores that are larger than the equilibrium GT size. For instance, a temperature shift down to −0.01 °C would cause the freezing of the pores larger than 3 μm, so the freezing of the pores at Mark A will not be shown in Figure 4. These ice-filled pores occupied around 13% of the total pore volume, and the QLL effect, as expected, was minor. This temperature drop is negligible in engineering, but shows remarkable impact on ice formation in macro pores, e.g., the pores in Mark A of the concrete sample. As temperature dropped further, the QLL effect rose. The ice fillings in the capillary pores (Mark B) and the gel pores (Mark C) can be reflected by the steeper plots of ice fraction against depressed temperature (Figure 4). For the cases of relatively small values of QLL thickness (e.g., d-1 and d-2), the similarly-shaped curves with the steep characteristic slopes at the same temperature intervals can be figured out. When the d-3 and d-4 models were used, the freezing of the water confined in the thin pores was significantly delayed or depressed. Obvious evidence was that the steep Stage B that initially began at around −0.4 °C was delayed to around −10 °C for the freezing of the water confined in the same pores with the very thick QLLs (Figure 4). Although those freezing delays were physically exaggerated because of the overestimated thickness values of the QLLs between the pore walls and the ice crystals by the d-3 and d-4 models, the results displayed in Figure 4 were mathematically reasonable. For instance, according to Equation (1), the pores with a width of 100 nm (radius of 50 nm) will freeze at −0.6 °C without the QLL effect, but the freezing temperature will be shifted to −8 °C with the QLL effect following the thickness model of d-4.

For comparison purposes, the experimental ice fractions of a concrete sample with the same water to cement ratio evaluated by the freezing and thawing phases of DSC measurement [43] are plotted in Figure 4. Due to the significant supercooling of water, ice crystals nucleated at −5 °C, then explosively grew in the pores that are larger than the GT size. After that, the ice growth that should be governed by the available pore water became much slower. At −20 °C, only 38% of the total pore water was frozen to ice, and it increased to 50% at −50 °C [43]. The ice fraction data from the thawing phase were slightly higher than those from the freezing phase after the nucleation stage (i.e., <−10 °C, Figure 4). The hysteresis of the ice fraction between freezing and thawing may come from the pore curvature-induced metastability of the confined phase, which is an intrinsic property of the pore system defined by the pore structure and the interfacial interactions [19]. Since the confined

thawing can avoid the supercooling effect, it generally approaches more closely the equilibrium case if the thawing speed is not very fast and thus is often adopted for pore structure measurement by cryoporometry [19,21]. The results plotted in Figure 4 show that the ice fraction curve with the QLL thickness of d-3 was close to that from the DSC thawing data [43]. However, this does not imply that the QLL thickness of d-3 dominated the intermediate QLL phase between the ice crystals and the pore walls of the concrete sample. As a matter of fact, two reasons may account for this observation. Firstly, the pore structure of the concrete sample may deviate from the real one since MIP only detects open pores in limited pore ranges (e.g., 3 nm in this study), and secondly, our estimation strictly relied on thermodynamic equilibrium, which cannot be achieved in either practice or rigorous experimental tests. Overall, the results displayed in Figure 4 indeed evidence the significant role QLL plays, and the integral understandings of this interfacial phase between ice crystals and substrates are wanted in the future.

4. Mechanical Consequences of Confined Freezing

4.1. Freezing Pressures

Once confined freezing takes place, the significant volume difference between ice and water will induce large hydraulic pressures on pore walls, which may mainly account for the frost damage in cement-based materials [23] and rocks [47], the frost heave in soils, and other relevant issues [3,48]. Here, we employed a simplified poroelastic model that involves the interactions among the ice, unfrozen water, and the material skeleton in the elastic regimes [24] to evaluate the hydraulic pressures. The effective hydraulic pressure over the pore-fluid domain in a porous material, $< P_d\phi >$, can be given by [24]:

$$< P_d\phi > \approx \frac{0.09K_s\,(1-\phi)^3\,\phi\phi_c}{2-2\phi^2+\phi^3} \tag{8}$$

where K_s is the bulk modulus of the material skeleton, and the constant 0.09 denotes the volume fraction change when water crystallizes to ice during freezing. When deducing Equation (8), the small density variations of ice and water were neglected, and the relation of $K = K_s(1-\phi)^3$ with K being the bulk modulus of the empty porous sample [49] was employed for exploring the porosity variation due to the deformation of the skeleton under pressure. Equation (8) indicates that the hydraulic pressure induced by the confined freezing was proportional to the ice content. Furthermore, softening the material skeleton will decrease the hydraulic pressure due to the fact that the deformations by the material itself can provide more space for pressure relaxation.

In addition to the hydraulic pressure, the crystallization process itself will also generate a pressure (termed as the crystallization pressure) on local pore walls even without volume change [50]. Unlike the hydraulic pressure that should be evenly and isotropically exerted on the entire pore system, the crystallization pressures acted on pore walls locally depending on the pore geometries and the depressed temperature. Therefore, the effective crystallization pressure over the ice-filled domain, $< P_c\phi_c >$, can be given by,

$$< P_c\phi_c >= \int_0^{\phi_c^{GT}} P_c d\phi_c \approx \sum (1-\lambda)\,\frac{\Delta H_f}{T_0}(T_0 - T_m)\Delta\phi_c \tag{9}$$

where ϕ_c^{GT} is the maximum equilibrium ice content according to the GT equation and λ is the shape factor, with $\lambda = 0.5$ and 1, respectively, representing the cylindrical and spherical pores [45]. An unsaturated freezing-thawing test suggested that the shape factor of concrete varied from 0.3–0.6 depending on the pore sizes [51]. In this study, $\lambda = 0.5$ was used, because the ice contents were calculated based on the pores of the cylinder.

Figure 5 displays the hydraulic and crystallization pressures estimated by Equations (8) and (9), respectively, based on the ice content data shown in Figure 4. During calculating, $K_s = 25$ GPa [52]

was used. As shown in Figure 5a, the significant hydraulic pressure shifts up to 14 MPa can be found immediately after the freezing begins (−0.01 °C). This can be due to the instantaneous ice filling in the macro-pores (Figure 4). For the cases of non-QLL and low QLL thickness values (d-1 and d-2), the hydraulic pressures accumulated continually, heavily, and rapidly as the temperature decreased down to −1 °C due to the large amount of ice forming in the capillary pores (Mark B in Figure 4). The further decreases in temperature to −6 °C remained promoting the hydraulic pressures, but at slower rates, owning to the delayed ice formation in the gel pores at nano-scales. After that, decreasing temperature only generated limited ice crystals due to the limited pore water for freezing, which consequentially accumulates only slight hydraulic pressures. For the thick QLL cases (d-3 and d-4), the hydraulic pressures augmented continually and consistently at relatively slow rates after the rapid rises at the beginning stage of freezing (Figure 5a). Those, again, were the consequences of ice formations in confined freezing that were sensitive to the QLL thickness (Figure 4). For example, due to the very depressed ice formation in the pores with the thick QLL of d-4, the final hydraulic pressure at −20 °C arrived at 36 MPa, only 40% of that without the QLL (88.5 MPa).

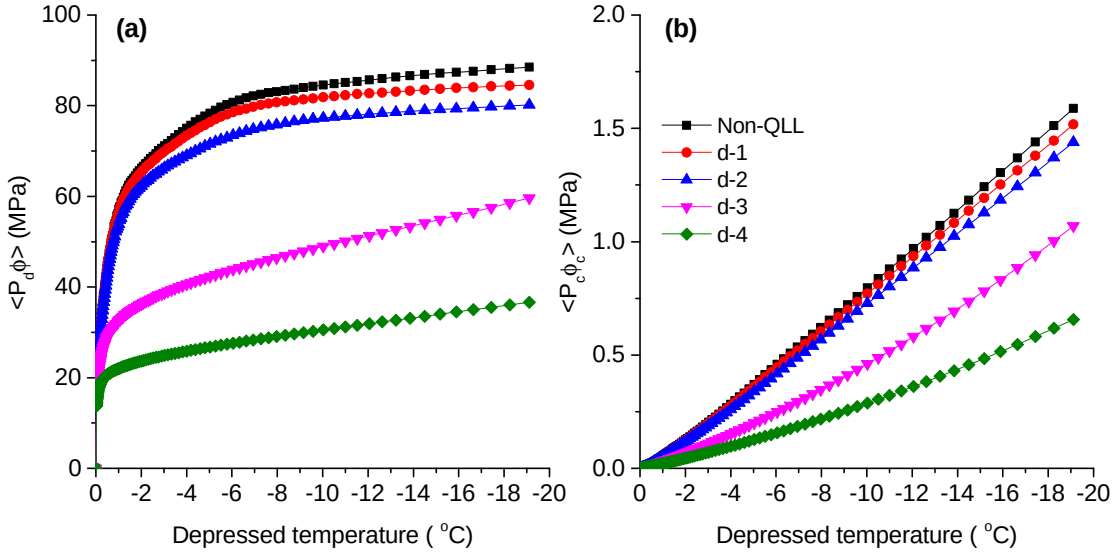

Figure 5. (**a**) Hydraulic pressures of confined freezing induced by the density change and (**b**) crystallization pressures induced by the curvature effect during freezing with different models of QLL thickness.

The crystallization pressures, unlike the hydraulic pressures that were primarily determined by the ice contents, showed different characteristics. Firstly, the crystallization pressures were far lower than the hydraulic pressures (less than 2 MPa; see Figure 5b). One shall understand that Equation (9) calculates the crystallization pressures that only work on locally-limited domains around ice crystals, which is different from the general expression without the working domains (e.g., $P_c \approx 1.2(T_0 - T_m)$ MPa [22,50]). Due to the very limited amount of the formed ice at each temperature decreasing step, the effective crystallization pressures were relatively small. Secondly, the crystallization pressures almost accumulated linearly with the temperature deceasing. This was intrinsically due to the algorithm of Equation (9), in which the weight factor $(T_0 - T_m)$ before $\Delta\phi_c$ always increased as the temperature deceased. However, the effect of QLL on the crystallization pressures remained similar to the hydraulic pressures, that is the thicker was the QLL, the lower were the pressures (Figure 5b).

Overall, the existence of QLL between ice crystals and pore walls tended to lower the effective hydraulic and crystallization pressures, and the former one was more sensitive to the amount and rate of ice accumulation in the confined freezing.

4.2. Links to Frost Deformations of Porous Materials

In order to bridge over the pressures that are generally exerted on local phases and the macro-deformations of porous materials that are integrally over the whole tested specimens, a poro-elastic approach [22,23,53,54] was employed. For a freely-deformable porous material without external restrictions, the linear deformation, ε, of the material under a subzero temperature can be given by,

$$\epsilon = \frac{< P_c \phi_c > + < P_d \phi >}{3K} + \alpha (T - T_0) \tag{10}$$

where α is the thermal expansion coefficient of the material. Here, $\alpha = 15.7 \times 10^{-6}$ (1/K) was estimated from the experimental data reported in [43].

Figure 6a shows the calculated freezing deformations of the concrete under freezing with the selected QLL thickness models. The material deformations were the direct consequences of the effective pore pressures (Figure 5). Clearly, the first freezing at the temperature shift down to -0.1 °C will cause the instantaneous expansions up to 3.3×10^{-4} mm/mm for all cases, which was indeed due to the rapidly raised hydraulic pressures up to 15 MPa (Figure 5). Those significant expansions continued as the ice accumulated in big pores (Segment A in Figure 6a). Later, the deformations with different QLL models diverged and grew according to the combined actions of the effective pore pressures and the thermal shrinkages. For the cases of non-QLL and low-thickness QLLs (d-1 and d-2), the deformation rising extents and rates decreased progressively as the temperature decreased (Segment B in Figure 6a), which was indeed due to the delayed ice formation in the capillary and gel pores. At the same time, the material always shrank with the temperature decreasing (see the solid line in Figure 6a). When the rises in pore pressure induced by the ice crystallization in fine pores could not compensate for the thermal shrinkages, the material began to shrink. In this study, shrinkages started (although insignificantly; see Segment C in Figure 6a and the acquired shrinkages in Figure 6b) when the temperature was lowered to -8 °C for the cases of non-QLL, d-1 and d-2. For the cases of d-3 and d-4, however, the material did not show shrinkages due to the fact that the freezing of the water confined in the capillary and gel pores was significantly delayed by the thick QLLs.

Figure 6a also displays the deformations of concrete upon freezing and thawing obtained from experimental measurements [43]. Four deformation segments can be singled out from the freezing deformation-temperature curve. A slight shrinkage occurred at $T > -1$ °C (Segment S in Figure 6) owning to the supercooling of the confined water that may be attributed to either the actions of the dissolved ions [44] or the natural kinetic-associated freezing process that requires a meta-stable status beyond the thermodynamic equilibria [25]. Later, in the temperature range between -1 °C and -2.6 °C, freezing deformation rose rapidly and significantly (Segment A') due to the ice formation in the coarse pores. Then, the deformation rise became less and slower between -2.6 °C and -7.5 °C (Segment B'), followed by a constantly increased, but rather minor deforming stage (Segment C') below -7.5 °C due to the continually-depressed ice formations. Roughly, the freezing deformations were close to the results of the non-QLL, d-1 and d-2 cases, predicted by the poroelastic analyses (Figure 6b), while the thawing data to those of d-3 and d-4 cases. This may inform that the poroelastic analysis can, to some extent, capture the physical regimes of confined freezing. Similar results were reported elsewhere [22,24]. However, large deviations between the experimental and predicted data can be observed at the early freezing stages. Specifically, the very first supercooling stage (Segment S) cannot be captured by the model because our predictions were strictly under thermodynamic equilibria and the pore water was only physically regulated by the curvature effect. The deviations from equilibrium cannot be avoided for a real freezing test, so the ice formation in any pore scale would always be delayed, which would cause biases between the predicted and measured deformations, as displayed in Figure 6. Indeed, the crystallization of the massive supercooled water in confined pores can cause a so-called thermal-shock effect that may bring additional damage to the porous material under freezing [55]. Another important reason accounting for the deformation deviations between the

experimental and modeled results may be the pore pressure relaxation that always occurs in the real freezing process of porous media [23,56], but was not considered here.

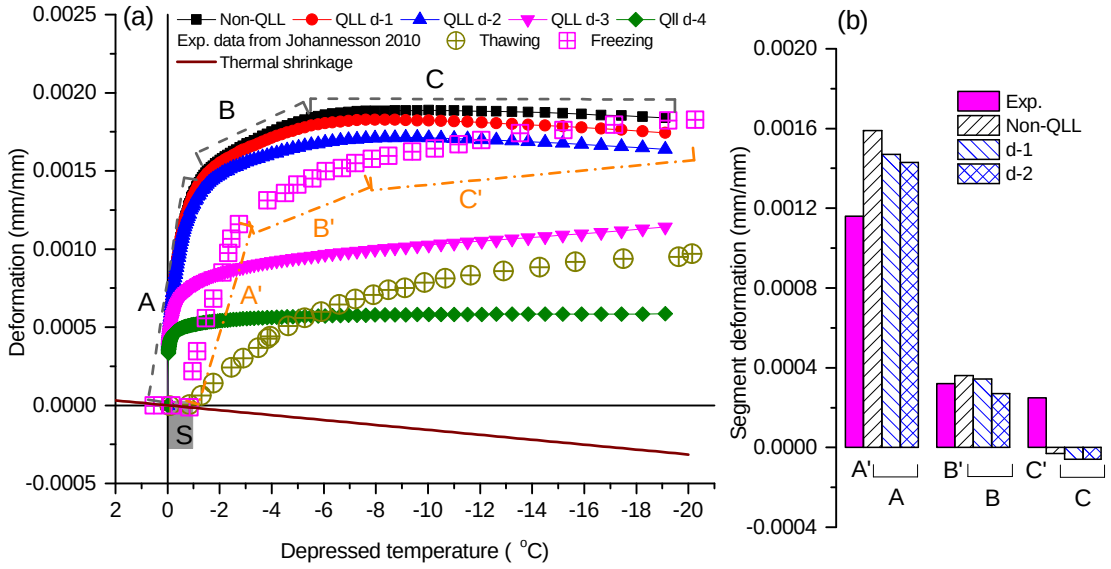

Figure 6. (**a**) Deformations of the concrete sample estimated by the poroelastic model with the different models of QLL thickness and the experimental results reported in [43]. In this figure, the experimental thawing data were corrected according to the set of $\epsilon = 0$ at $T = T_0$. Three segments of the modeled freezing deformations with different rising extents are marked as A, B, and C to represent the significant, moderate, and slight deformation rises by the delayed ice formation in different pores. The same freezing stages for the experiment data are marked as A′, B′, and C′, respectively. The process of supercooling monitored by the experiments is marked as S. (**b**) The comparison of the deformations at each segment between the experimental data and the predicted results in the non- and low-thickness QLL cases (d-1 and d-2).

Despite the acceptable agreements between the experimental and predicted deformations, some important issues that are intimately related to the complex confined freezing, but have not been fully addressed in the present study deserve further discussion. Firstly, the thermodynamic and structurally-configurational properties of the water and ice confined in nanopores were assumed to be the same as those of the bulk phases. This assumption may be challenged by the disordered structure of ice and water by the actions of pore walls [18]. For instance, it was reported that water in nanopores freezes to cubic ice instead of hexagonal ice with lower free energy [15,16]. Secondly, the possible influences of high pressure on the structure and physical properties of the confined water, ice, and QLLs were not considered here, while the increasingly-reported evidence has supported that high pressures can substantially change the crystal structures of ice and its growth mechanisms [17,57]. Thirdly, the pore structure of cement-based materials is far more complex than the grade cylinders as assessed by the MIP method. Our previous studies indicated that the pores (and their surfaces) in cement-based materials are constructed in "chaos" (or fractal) patterns [26]. Theoretical analyses showed that fractal substrates can substantially impact the nucleation rate and crystal size [58–60]. For a material with such complex pores, the local curvature effect may further influence local ice structures and, consequentially, freezing kinetics and the stresses generated [61,62]. Last but not least, our predictions were carried out under the elastic regime, in which all phases deformed elastically and linearly with the pressures generated by different sources. Local pressures (e.g., crystallization pressures) were homogenized into some pattern (Equation (9)) to get the integral body stresses, which may be too simple to represent the real stress field in the material. Deepened understandings of the influences of those issues on the ice-QLL-substrate system and the engineering consequences deserve further rigorous investigations in the future.

5. Conclusions

- The intermediate phase, QLL, with a structure different from ice and water, exists to stabilize the ice exposed to different media or in contact with different substrates under freezing. The thickness of QLL generally decays with the temperature decreasing, which can be captured by the thermodynamic models with the long-and short-range interactions between the ice and the substrate.
- Four different models of QLL thickness were representatively employed to correct the GT equation and to address its effect on the ice content of a concrete sample, whose pore structure was determined by MIP. Under thermodynamic equilibria, the concrete with broad PSD at multiple scales showed the unevenly rising extents and rates of ice against the depressed temperature. The thickened QLL can delay the freezing temperature and depress the ice content of the water confined in the pores.
- When confined freezing occurs in a porous material, the hydraulic pressures due to the volume difference between ice and water build up depending on the pore structure and material properties. The crystallization pressures that are generated by the penetration of ice into thin pores almost increase linearly with the depressed temperature. Both pressures decrease with thickening of the QLL.
- The freezing deformations of porous materials depend on the effective pore pressures built by the confined freezing and the thermal shrinkages during freezing. The QLL corrections seem to mitigate the deviations between the predicted and measured freezing deformations. The underlined physical regimes are indeed associated with the QLL-associated ice content in freezing pores, and some related issues remain to be advanced in the future.

Author Contributions: Q.Z. and K.L. contributed equally to this work.

Funding: The research was funded by the National Natural Science Foundation of China (Nos. 51878602 and 51778332).

Acknowledgments: The authors acknowledge the anonymous reviewers to improve the quality of this study.

Conflicts of Interest: The authors declare no conflict of interest.

Appendix A

The free energy changes $\Delta G(T,t)$ of the representative water-filled pore before and after freezing, which depend on the temperature T and QLL thickness t, can be given by,

$$\Delta G(T,t) = \underbrace{\frac{T-T_0}{T_0}\Delta H_f V_c}_{\text{Freezing heat}} + \underbrace{\gamma_{lc}A_c}_{\text{New surface}} + \underbrace{\Delta\gamma A_p F(t)}_{\text{Disturbance in surface energy}} \quad \text{(A1)}$$

Note that Equation (A1) is different from the generally used expression that only involves the local surface-energy changes by the intermediate phase ($\Delta G(T,t) = \gamma_{lc} + \Delta\gamma F(t)$) [3]. More discussions about Equation (A1) can be found elsewhere [3,4,27].

Since the intermediate QLL is generated to stabilize the ice-solid system, the total free energy is required to be minimal in equilibrium. The partial derivative of $\Delta G(T,t)$ with respect to t was then conducted in Equation (A1), which yields,

$$\frac{\partial \Delta G(T,t)}{\partial t} = 0 = -A_p\left[\frac{T-T_0}{T_0}\Delta H_f\left(1-2\kappa t\right) + 2\kappa\gamma_{lc} - \Delta\gamma\frac{\partial F(t)}{\partial t}\right] \quad \text{(A2)}$$

When deducing Equation (A2), the relations, $\partial V_c/\partial t = -A_p\left(1-2\kappa t\right)$ and $\partial A_c/\partial t = -2\kappa A_p$ from Equation (2), were used. Considering further the limited contribution of the QLL (i.e., $2\kappa t \ll 1$) and the GT equation (Equation (1)), Equation (A2) reduces to $\partial F/\partial t = \Delta H_f\left(T-T_m\right)/\Delta\gamma T_0$. This relation reveals that the differential interfacial potential against thickness is primarily determined by

the changes in temperature ($T - T_m$). Estimating the thickness of QLL relies on how the interfacial potential $F(t)$ is chosen, although the required parameters may vary conditionally (e.g., $\Delta\gamma$).

References

1. Furukawa, Y. Snow and ice crystal growth. In *Handbook of Crystal Growth*, 2nd ed.; Elsevier Science: Amsterdam, The Netherlands, 2015; pp. 1061–1112.
2. Murata, K.; Asakawa, H.; Nagashima, K.; Furukawa, Y.; Sazaki, G. Thermodynamic origin of surface melting on ice crystals. *Proc. Natl. Acad. Sci. USA* **2016**, *113*, E6741–E6748. [CrossRef]
3. Dash, J.G.; Rempel, A.W.; Wettlaufer, J.S. The physics of premelted ice and its geophysical consequences. *Rev. Mod. Phys.* **2006**, *78*, 695–741. [CrossRef]
4. Limmer, D.T. Closer look at the surface of ice. *Proc. Natl. Acad. Sci. USA* **2016**, *113*, 12347–12349. [CrossRef]
5. Mochizuki, K.; Molinero, V. Antifreeze glycoproteins bind reversibly to ice via hydrophobic groups. *J. Am. Chem. Soc.* **2018**, *140*, 4803–4811. [CrossRef] [PubMed]
6. Doppenschmidt, A.; Butt, H.J. Measuring the thickness of the liquid-like layer on ice surfaces with atomic force microscopy. *Langmuir* **2000**, *16*, 6709–6714. [CrossRef]
7. Limmer, D.T.; Chandler, D. Premelting, fluctuations, and coarse-graining of water-ice interfaces. *J. Chem. Phys.* **2014**, *141*, 18C505. [CrossRef]
8. Bluhm, H.; Ogletree, D.F.; Fadley, C.S.; Hussain, Z.; Salmeron, M. The premelting of ice studied with photoelectron spectroscopy. *J. Phys. Condens. Matter* **2002**, *14*, L227. [CrossRef]
9. Liljeblad, J.F.; Furo, I.; Tyrode, E.C. The premolten layer of ice next to a hydrophilic solid surface: Correlating adhesion with molecular properties. *Phys. Chem. Chem. Phys.* **2017**, *19*, 305–317. [CrossRef] [PubMed]
10. Conde, M.M.; Vega, C.; Patrykiejew, A. The thickness of a liquid layer on the free surface of ice as obtained from computer simulation. *J. Chem. Phys.* **2008**, *129*, 014702. [CrossRef]
11. Furukawa, Y.; Nada, H. Anisotropic surface melting of an ice crystal and its relationship to growth forms. *J. Phys. Chem. B* **1997**, *101*, 6167–6170. [CrossRef]
12. Dosch, H.; Lied, A.; Bilgram, J.H. Glancing-angle X-ray scattering studies of the premelting of ice surfaces. *Surf. Sci.* **1995**, *327*, 145–164. [CrossRef]
13. Carrasco, J.; Hodgson, A.; Michaelides, A. A molecular perspective of water at metal interfaces. *Nat. Mater.* **2012**, *11*, 667–674. [CrossRef]
14. Dash, J.G.; Fu, H.; Wettlaufer. J.S. The premelting of ice and its environmental consequences. *Rep. Prog. Phys.* **1995**, *58*, 115–167. [CrossRef]
15. Han, Y.Y.; Shuai, J.; Lu, H.M.; Meng, X.K. Size- and dimensionality-dependent thermodynamic properties of ice nanocrystals. *J. Phys. Chem. B* **2012**, *116*, 1651–1654. [CrossRef] [PubMed]
16. Jelassi, J.; Castricum, H.L.; Bellissent-Funel, M.C.; Dore, J.; Webber, J.B.W.; Sridi-Dorbez, R. Studies of water and ice in hydrophilic and hydrophobic mesoporous silicas: Pore characterisation and phase transformations. *Phys. Chem. Chem. Phys.* **2010**, *12*, 2838–2849. [CrossRef] [PubMed]
17. Nada, H. Analysis of ice crystal growth shape under high pressure using molecular dynamics simulation. *Cryst. Growth Des.* **2011**, *11*, 3130–3136. [CrossRef]
18. Bjorneholm, O.; Hansen, M.H.; Hodgson, A.; Liu, L-M..; Limmer, D.T.; Michaelides, A.; Pedevilla, P.; Rossmeisl, J.; Shen, H.; Tocci, G.; et al. Water at interfaces. *Chem. Rev.* **2016**, *116*, 7698–7726. [CrossRef]
19. Petrov, O.V.; Furo, I. NMR cryoporometry: Principles, applications and potential. *Prog. Nucl. Magn. Reson. Spectrosc.* **2009**, *54*, 97–122. [CrossRef]
20. Sun, Z.; Scherer, G.W. Pore size and shape in mortar by Themoporosimetry. *Cem. Concr. Res.* **2010**, *40*, 740–751. [CrossRef]
21. Mitchell, J.; Webber, J.B.W.; Strange, J.H. Nuclear magnetic resonance cryoporometry. *Phys. Rep.* **2008**, *461*, 1–36. [CrossRef]
22. Zeng, Q.; Fen-Chong, T.; Li, K. Freezing behavior of cement pastes saturated with NaCl solution. *Constr. Build. Mater.* **2014**, *59*, 99–110. [CrossRef]
23. Zeng, Q.; Fen-Chong, T.; Dangla, P.; Li, K. A study of freezing behavior of cementitious materials by poromechanical approach. *Int. J. Solid Struct.* **2011**, *48*, 3267–3273. [CrossRef]

24. Zeng, Q.; Li, K.; Fen-Chong, T. Elastic behavior of saturated porous materials under undrained freezing. *Acta Mech. Sin.* **2013**, *29*, 827–835. [CrossRef]
25. Zeng, Q.; Li, K.; Fen-Chong, T. Heterogeneous nucleation of ice from supercooled NaCl solution confined in porous cement paste. *J. Cryst. Growth* **2015**, *409*, 1–9. [CrossRef]
26. Zeng, Q.; Luo, M.; Pang, X.; Li, L.; Li, K. Surface fractal dimension: An indicator to characterize the microstructure of cement-based porous materials. *Appl. Surf. Sci.* **2013**, *282*, 302–307. [CrossRef]
27. Petrov, O.V.; Vargas-Florencia, D.; Furo, I. Surface melting of octamethylcyclotetrasiloxane confined in controlled pore glasses: Curvature effects observed by 1H NMR. *J. Phys. Chem. B* **2007**, *111*, 1574–1581. [CrossRef]
28. Likos, C.N.; Mecke, K.R.; Wagner, H. Statistical morphology of random interfaces in microemulsions. *J. Chem. Phys.* **1995**, *102*, 9350–9361. [CrossRef]
29. Golecki, I.; Jaccard, C. Intrinsic surface disorder in ice near the melting point. *J. Phys. C Solid State Phys.* **1978**, *11*, 4229–4237. [CrossRef]
30. Wettlaufer, J.S.; Worster, M.G.; Wilen, L.A.; Dash, J.G. A theory of premelting dynamics for all power law forces. *Phys. Rev. Lett.* **1996**, *76*, 3602–3605. [CrossRef]
31. Fagerlund, G. Determination of pore-size distribution from freezing-point depression. *Mater. Struct.* **1973**, *6*, 215–225. [CrossRef]
32. Brun, M.; Lallemand, A.; Quinson, J.F.; Eyraud, C. A new method for the simultaneous determination of the size and the shape of pores: The thermoporometry. *Thermochim. Acta* **1977**, *21*, 59–88. [CrossRef]
33. Goertz, M.P.; Zhu, X.Y.; Houston, J.E. Exploring the liquid-like layer on the ice surface. *Langmuir* **2009**, *25*, 6905–6908. [CrossRef]
34. Sadtchenko, V.; Ewing, G.E. Interfacial melting of thin ice films: An infrared study. *J. Chem. Phys.* **2002**, *116*, 4686–4697. [CrossRef]
35. Elbaum, M.; Lipson, S.G.; Dash, J.G. Optical study of surface melting on ice. *J. Cryst. Growth* **2002**, *129*, 491–505. [CrossRef]
36. Gilpin, R.R. Theoretical studies of particle engulfment. *J. Colloid Interface Sci.* **1980**, *74*, 44–63. [CrossRef]
37. Engemann, S.; Reichert, H.; Dosch, H.; Bilgram, J.; Honkimaki, V.; Snigirev, A. Interfacial melting of ice in contact with SiO_2. *Phys. Rev. Lett.* **2004**, *92*, 205701. [CrossRef]
38. Jahnert, S.; Vaca Chavez, F.; Schaumann, G.E.; Schreiber, A.; Schonhoff, M.; Findenegg, G.H. Melting and freezing of water in cylindrical silica nanopores. *Phys. Chem. Chem. Phys.* **2008**, *10*, 6039–6051. [CrossRef] [PubMed]
39. Cahn, J.W.; Dash, J.G.; Fu, H. Theory of ice premelting in monosized powders. *J. Cryst. Growth* **1992**, *123*, 101–108. [CrossRef]
40. Washburn, E.W. Note on a method of determining the distribution of pore sizes in a porous material. *Proc. Natl. Acad. Sci. USA* **1921**, *7*, 115–116. [CrossRef]
41. Jiang, C.; Guo, W.; Chen, H.; Zhu, Y.; Jin, C. Effect of filler type and content on mechanical properties and microstructure of sand concrete made with superfine waste sand. *Constr. Build. Mater.* **2018**, *192*, 442–449. [CrossRef]
42. Muller, A.C.A.; Scrivener, K.L. A reassessment of mercury intrusion porosimetry by comparison with 1H NMR relaxometry. *Cem. Concr. Res.* **2017**, *100*, 350–360. [CrossRef]
43. Johannesson, B. Dimensional and ice content changes of hardened concrete at different freezing and thawing temperatures. *Cem. Concr. Compos.* **2010**, *32*, 73–83. [CrossRef]
44. Wu, M.; Johannesson, B.; Geiker, M. A preliminary study of the influence of ions in the pore solution of hardened cement pastes on the porosity determination by low temperature calorimetry. *Thermochim. Acta* **2014**, *589*, 215–225. [CrossRef]
45. Wang, Z.; Zeng, Q.; Wu, Y.; Wang, L.; Yao, Y.; Li, K. Relative humidity and deterioration of concrete under freeze–thaw load. *Constr. Build. Mater.* **2014**, *62*, 18–27. [CrossRef]
46. Fabbri, F.; Fen-Chong, T. Indirect measurement of the ice content curve of partially frozen cement based materials. *Cold Reg. Sci. Technol.* **2013**, *90–91*, 14–21. [CrossRef]
47. Huang, S.; Liu, Q.; Liu, Y.; Ye, Z.; Cheng, A. Freezing strain model for estimating the unfrozen water content of saturated rock under low temperature. *Int. J. Geomech.* **2018**, *18*, 04017137. [CrossRef]

48. Bartels-Rausch, T.; Jacobi, H.W.; Kahan, T.F.; Thomas, J.L.; Thomson, E.S.; Abbatt, J.P.D.; Ammann, M.; Blackford, J.R.; Bluhm, H.; Boxe, C.; et al. A review of air–ice chemical and physical interactions (AICI): Liquids, quasi-liquids, and solids in snow. *Atmos. Chem. Phys.* **2014**, *14* 1587–1633. [CrossRef]
49. Fen-Chong, T.; Fabbri, A.; Thiery, M.; Dangla, P. Poroelastic analysis of partial freezing in cohesive porous materials. *J. Appl. Mech.* **2013**, *80*, 020910. [CrossRef]
50. Scherer, G.W. Crystallization in pores. *Cem. Concr. Res.* **1999**, *29*, 1347–1358. [CrossRef]
51. Wang, Z.; Zeng, Q.; Wang, L.; Yao, Y.; Li, K. Effect of moisture content on freeze–thaw behavior of cement paste by electrical resistance measurements. *J. Mater. Sci.* **2014**, *49*, 4305–4314. [CrossRef]
52. Ghabezloo, S. Association of macroscopic laboratory testing and micromechanics modelling for the evaluation of the poroelastic parameters of a hardened cement paste. *Cem. Concr. Res.* **2010**, *40*, 1197–1210. [CrossRef]
53. Coussy, O. Poromechanics of freezing materials. *J. Mech. Phys. Solids* **2005**, *53*, 1689–1718. [CrossRef]
54. Liu, L.; Qin, S.; Wang, X. Poro-elastic—Plastic model for cement-based materials subjected to freeze-thaw cycles. *Constr. Build. Mater.* **2018**, *184*, 87–99. [CrossRef]
55. Demirdag, S. Effects of freezing-thawing and thermal shock cycles on physical and mechanical properties of filled and unfilled travertines. *Constr. Build. Mater.* **2013**, *47*, 1395–1401. [CrossRef]
56. Coussy, O.; Fen-Chong, T. Crystallization, pore relaxation and micro-cryosuction in cohesive porous materials. *CR Mec.* **2005**, *333*, 507–512. [CrossRef]
57. Suh, D.; Yasuoka, K. Heterogeneous cavitation and crystallisation with an impurity by molecular dynamics. *Mol. Simul.* **2018**, *44*, 530–533. [CrossRef]
58. Zeng, Q. A simple method for estimating the size of nuclei on fractal surfaces. *J. Cryst. Growth* **2017**, *475*, 49–54. [CrossRef]
59. Yan, D.; Zeng, Q.; Xu, S.; Zhang, Q.; Wang, J. Heterogeneous nucleation on concave rough surfaces: Thermodynamic analysis and implications for nucleation design. *J. Phys. Chem. C* **2016**, *120*, 10368–10380. [CrossRef]
60. Zeng, Q.; Xu, S. Thermodynamics and characteristics of heterogeneous nucleation on fractal surfaces. *J. Phys. Chem. C* **2015**, *119*, 27426–27433. [CrossRef]
61. Morishige, K. Influence of pore wall hydrophobicity on freezing and melting of confined water. *J. Phys. Chem. C* **2018**, *122*, 5013–5019. [CrossRef]
62. Kastelowitz, N.; Molinero, V. Ice-liquid oscillations in nanoconfined water. *ACS Nano* **2018**, *12*, 8234–8239. [CrossRef] [PubMed]